
Article:
Xu, J., Odavic, M. orcid.org/0000-0002-2104-8893, Zhu, Z. orcid.org/0000-0001-7175-3307 et al. (2 more authors) (2021) A generalized decomposition model of dual three-phase permanent magnet synchronous machines considering asymmetric impedances and compensation capability. IEEE Transactions on Industry Applications, 57 (4). pp. 3763-3775. ISSN 0093-9994

https://doi.org/10.1109/tia.2021.3077525

A Generalized Decomposition Model of Dual Three-Phase Permanent Magnet Synchronous Machines Considering Asymmetric Impedances and Compensation Capability

Jin Xu, Milijana Odavic, *Member*, *IEEE*, Zi-Qiang Zhu, *Fellow*, *IEEE*, Zhan-Yuan Wu, and Nuno Freire

***Abstract*— This paper firstly proposes a generalized decomposition model for dual three-phase (3-ph) permanent magnet synchronous machines (PMSMs) with 0°, 30°, and 60° angle displacements between two sets of windings, allowing machines controlled in two-dimensional orthogonal αβ and xy subspaces. This model can decouple mutual inductances coupling phases from two sets, respectively. However, there often exist asymmetric impedances, due to inherent asymmetric machine parameters, cables with unequal lengths, manufacture tolerances, etc., in dual 3-ph PMSMs inevitably causing unbalanced phase currents and deteriorating the decoupling performance of the generalized machine model. Therefore, the generalized decomposition model incorporating asymmetric impedances is further developed, in which additional terms incurred by asymmetric impedances lead to the cross-coupling of αβ subspace and xy subspace. Through this model, the compensation capability of asymmetries is derived at a given DC link voltage. Then, a compensation strategy is illustrated to suppress unbalanced phase currents together with current harmonics caused by nonlinearities. Finally, experimental results testify the current balancing performance and simulation results further validate the machine model and the compensation capability.**

***Index Terms*— Asymmetric impedances, Dual three-phase permanent magnet synchronous machine, Generalized decomposition model.**

I. Introduction

Dual three-phase (3-ph) permanent magnet synchronous machines (PMSMs) are increasingly popular in industrial applications, such as electric ship propulsion, electrical vehicles, wind generators, aerospace, etc. [1]-[3], due to additional degrees of freedom [4], high-power low-current capability, high torque density, and other benefits. It is acknowledged angle displacement (AD) between two sets of windings is one of the key factors, determining the machine performance [5]-[6]. Among various ADs, 0°, 30°, and 60° ADs are widely used, as shown in Fig. 1. The machine design schematics of these three main types of dual 3-ph machines can be found in [6]-[8] (0°-AD), [5], [9]-[13] (30°-AD) and [13]-[14] (60°-AD), respectively.

For the 0°-AD machine, due to the character of no angle displacement between two sets of 3-ph windings, the hardware or software can be identical for control of the two sets of 3-ph windings, which makes the system more interchangeable and increases the system redundancy. This could be desirable for an industrial product such as that in a megawatt wind turbine generator. Meanwhile, the 0°-AD machine is illustrated to have advantages to reduce the short-circuit current at fault operations [7]. On the other hand, the topology of the 0°-AD machine allows tests of the machine or converter up to the full load without requiring additional facilities by arranging the two sets operating at motor and generator modes, respectively [8]. For 30°-AD machines, they can offer a lower torque ripple [5], [12], and fewer MMF harmonic components [5], compared with 60°-AD machines. However, the amplitudes of these harmonic components should be analyzed in specific applications [5]. On the other hand, the slot/pole combinations and winding types play significant roles in the performances of 30°/60°-AD machines [5]. There is also an application of 60°-AD machines for the electrical power steering system [14]. In summary, 0°, 30°, and 60° angle displacements are common choices for dual 3-ph PMSMs and the angle displacement can be chosen according to the specific application requirements.

For the dual 3-ph PMSMs with two neutral points not connected shown in Fig. 1, the two sets of windings can be controlled separately [15]-[17]. However, these two sets are not independent due to mutual inductances coupling phases from two sets, respectively, which means one dual 3-ph PMSM cannot be simply viewed as a combination of two single 3-ph PMSMs. Therefore, vector space decomposition (VSD) is introduced in [18] for 30°-AD dual 3-ph PMSMs which can solve the coupling issue of mutual inductances mentioned previously. In VSD, components of different orders are decoupled into two orthogonal subspaces, which facilitates the regulation of fundamental and harmonic order components separately [19]. Similarly, 60°-AD dual 3-ph PMSMs can be considered as symmetrical six-phase machines and the decoupling matrix shown in [20] can decouple the mutual

This work was supported by the UK EPSRC Prosperity Partnership "A New Partnership in Offshore Wind" under Grant No. EP/R004900/1."

Jin Xu, Milijana Odavic, and Zi-Qiang Zhu are with Department of Electronic and Electrical Engineering, University of Sheffield, S10 2TN Sheffield, U.K. (e-mail: jxu60@sheffield.ac.uk; m.odavic@sheffield.ac.uk; z.q.zhu@sheffield.ac.uk). Zhan-Yuan Wu is with Sheffield Siemens Gamesa Renewable Energy Research Centre, S10 2TN Sheffield, U.K. (e-mail: Zhan-Yuan.Wu@siemensgamesa.com). Nuno Freire is with Siemens Gamesa Renewable Energy AS, 7330 Brande, Denmark. (e-mail: Nuno.Freire@siemensgamesa.com).

inductances. However, the solution for 0°-AD dual 3-ph PMSMs is still not addressed in the literature. Therefore, a decomposition approach of 0°-AD dual 3-ph PMSMs is required.

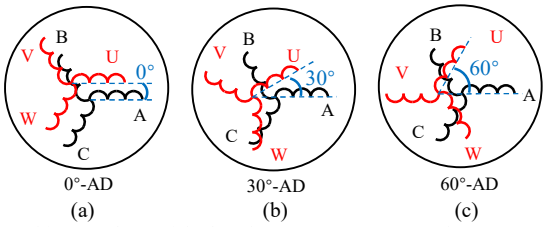

Fig. 1 Machine topology of dual 3-ph PMSMs. (a) 0°-AD. (b) 30°-AD. (c) 60°-AD.

On the other hand, the decomposition machine models for 30°-AD and 60°-AD dual 3-ph PMSMs mentioned in [18], [20] are established on the premise of symmetrical impedances (ideal condition), thereby resulting a totally decoupled two subspaces (αβ and xy subspaces) facilitating the control design. However, the existing asymmetric impedances can lead to coupling terms between αβ and xy subspaces. The asymmetric impedances can be classified into three main categories, i.e. partially coupled mutual inductances, asymmetric resistances, and asymmetric self-inductances. The partially coupled mutual inductances in dual 3-ph PMSMs can be caused by inherent machine parameters, for example, by designing the modular stator structure [10]). Normally, asymmetric resistances and self-inductances can be caused by cables with unequal lengths connecting phase terminals of the machine to the converter [21], different phase winding temperatures [22], manufacturing tolerances, etc. Meanwhile, the large asymmetric resistances and self-inductances would occur when there is a short circuit in turns of stator windings [23].

Therefore, the asymmetric impedances could commonly exist in drive systems of dual 3-ph PMSMs. Without compensation, there would be unbalanced phase currents [21], [24]-[27], leading to the increase of torque ripple and machine losses [28]. To compensate the unbalanced phase currents in the control scheme based on the decomposition model, the influences of asymmetric impedances on the decomposition machine models deserve a systematic investigation that benefits the development of compensation strategies and the derivation of the compensation capability. The compensation capability is of importance because it indicates whether the system is able to compensate the asymmetric impedances.

The modeling approaches of asymmetric impedances for 3-ph machines/inverters are addressed in publications [29]-[30]. For 3-ph systems, a generalized model of the PWM rectifier system separating the positive and negative sequences can describe the influences of an unbalanced network [29]. Proportions of positive and negative sequences reflected the unbalanced severity. Similarly, in [30] a unified mathematical model containing positive and negative synchronously rotating frames can describe a voltage-sourced converter-based drive system under an unbalanced grid supply and unbalanced input impedances. In terms of dual 3-ph machines, literature mainly covers 30°-AD machines [24]-[25], [31]-[32]. In [31] an analytical model of a dual 3-ph induction machine with one phase open is illustrated with additional terms caused by the open-loop phase. In [24], different values of the stator resistances and stator leakage inductances of two stator branches in dual 3-ph induction machines are presented in the developed machine model by two coefficients. However, the asymmetric impedances for phases within one branch are not involved. In [25], the fundamental current in xy subspace caused by unbalanced parameters can be specified into positive and negative sequences without mentioning the detailed machine model affected by asymmetric impedances.

As mentioned, the main result of asymmetric impedances is unbalanced phase currents. Approaches to balance phase currents can be generally classified into external hardware addition [21], [26] and software current balancing [30], [25], [27], [32]-[33]. Unbalanced phase currents can be suppressed through a calculated circuit containing resistances and inductances [26]. Apart from additional hardware, current regulation approaches, such as PI [25], proportional-resonant (PR) controllers [30], proportional-integral-resonant controllers (PIR) [32], model predictive control [33], are testified a good performance to balance phase currents caused by asymmetric impedances or loads. Furthermore, typical current controllers (PI, PR, and PIR) are compared theoretically in the aspect of performance of current balancing in [27]. However, whether the drive system or the DC link has the capability to provide the voltage to compensate the unbalanced currents caused by asymmetric impedances should be assured before compensation. To achieve this, the analysis of the influences of asymmetric impedances on the decomposition model showing additional coupling terms, more explicit and detailed than positive/negative sequences mentioned in the literature [25], [29]-[30], is required. Meanwhile, all three main categories, i.e. partially coupled mutual inductances, asymmetric resistances, and asymmetric self-inductances, should be covered.

This paper is further developed from [34]. In [34], a generalized decomposition model for 0°, 30°, and 60°-AD dual 3-ph PMSMs can solve the mutual inductance coupling issue of phases from two sets, respectively, but asymmetric impedances are not considered. After a brief introduction of the generalized decomposition model in Section II, additional coupling terms in this generalized decomposition model caused by asymmetric impedances are analyzed in detail in Section III. The compensation capability of asymmetries restricted by DC link voltage in the drive system can be derived from the developed model considering asymmetric impedances. Afterwards, an approach to compensate impedance asymmetries is illustrated in Section IV, followed by experimental validation on a direct-drive wind power test rig in Section V. Furthermore, the model considering impedance asymmetries and the compensation capability is validated through simulation in Section VI.

II. Generalized Decomposition Model of 0°, 30°, and 60°-AD Dual 3-ph PMSMs

In this section, the original machine model of 0°, 30°, and 60°-AD dual 3-ph PMSM in the stationary reference frame is shown first. Then, the generalized decomposition model is developed from the original machine model.

A. Machine Model in Stationary Reference Frame

Assuming that there are no iron saturation effects and iron losses, the original machine model in stationary reference frame for 0°, 30°, and 60°-AD dual 3-ph PMSMs can be expressed as

$$\begin{cases} \boldsymbol{u_s} = \boldsymbol{R_s i_s} + \dfrac{d\boldsymbol{\psi_s}}{dt} \\ \boldsymbol{\psi_s} = \boldsymbol{L_s i_s} + \boldsymbol{\gamma_s}\psi_{fd} \end{cases}, \tag{1}$$

in which

$$\begin{cases} \boldsymbol{u_s} = [u_A \quad u_U \quad u_B \quad u_V \quad u_C \quad u_W]^{\mathrm{T}} \\ \boldsymbol{i_s} = [i_A \quad i_U \quad i_B \quad i_V \quad i_C \quad i_W]^{\mathrm{T}} \\ \boldsymbol{\psi_s} = [\psi_A \quad \psi_U \quad \psi_B \quad \psi_V \quad \psi_C \quad \psi_W]^{\mathrm{T}} \\ \boldsymbol{R_s} = \mathrm{diag}[R_A \quad R_U \quad R_B \quad R_V \quad R_C \quad R_W] \\ \boldsymbol{\gamma_s} = [\cos\theta_e \quad \cos(\theta_e - \theta_{AU}) \quad \cos(\theta_e - \theta_{AB}) \\ \quad \cos(\theta_e - \theta_{AV}) \quad \cos(\theta_e - \theta_{AC}) \quad \cos(\theta_e - \theta_{AW})]^{\mathrm{T}} \\ \boldsymbol{L_s} = L_\sigma \boldsymbol{I_6} \\ \quad + \begin{bmatrix} M_{AA} & M_{AU} & M_{AB} & M_{AV} & M_{AC} & M_{AW} \\ M_{AU} & M_{UU} & M_{BU} & M_{UV} & M_{CU} & M_{UW} \\ M_{AB} & M_{BU} & M_{BB} & M_{BV} & M_{BC} & M_{BW} \\ M_{AV} & M_{UV} & M_{BV} & M_{VV} & M_{CV} & M_{VW} \\ M_{AC} & M_{CU} & M_{BC} & M_{CV} & M_{CC} & M_{CW} \\ M_{AW} & M_{UW} & M_{BW} & M_{VW} & M_{CW} & M_{WW} \end{bmatrix} \end{cases}, \tag{2}$$

where ψ_{fd} — rotor flux linkage;
u_A, u_B, u_C, u_U, u_V, u_W — phase voltages;
i_A, i_B, i_C, i_U, i_V, i_W — phase currents;
ψ_A, ψ_B, ψ_C, ψ_U, ψ_V, ψ_W — flux linkages;
R_A, R_B, R_C, R_U, R_V, R_W— phase resistances;
θ_e — electrical angle;
θ_{AN} (N=B, C, U, V, W) — electrical angle displacement between Phase A and Phase N;
L_σ — leakage inductance;
M_{KL} (K, L = A, B, C, U, V, W) — mutual inductance between Phase K and Phase L. If K and L are the same, it denotes the self-inductance.

B. Generalized Decomposition Model

If two sets of 3-ph windings are modelled and controlled separately, mutual inductances between phases from two sets, respectively, such as M_{AU}, M_{AV} in (1) are neglected, leading to imprecision. However, these mutual inductances are decoupled in the generalized decomposition machine model. Another benefit is to regulate the fundamental component and main harmonics separately in two subspaces. Thus, the αβ subspace producing electromagnetic torque and harmonics-related xy subspace can be separately regulated.

It is assumed that all resistances and self-inductances are symmetrical and mutual inductances are fully coupled. To simplify the decomposition and the analysis of influences of asymmetric impedances on the decomposition model, the high-order harmonics of the magnetic field in the air gap conventionally with relatively small amplitudes are neglected and the dominant fundamental component is considered exclusively. Then, impedances in (2) can be simplified by

$$\begin{cases} R_s = R_A = R_B = R_C = R_U = R_V = R_W \\ M_1 = M_{AA} = M_{BB} = M_{CC} = M_{UU} = M_{VV} = M_{WW} \\ M_{KL} = M_1 \cdot \cos(\theta_{KL}) \ \ (K, L = A, B, C, U, V, W; K \neq L) \end{cases}, \tag{3}$$

in which, R_s and M_1 are the nominal value of resistances and self-inductances, respectively; θ_{KL} denotes the electrical angle shift between Phase K and Phase L.

From (3), it is noted that mutual inductance M_{KL} is dependent on the AD of machines. Then, the decomposition matrices for 0°, 30°, and 60°-AD dual 3-ph PMSMs are classified as

$$\boldsymbol{D_v} = \begin{cases} \boldsymbol{D_{v0,60}}, (0^\circ/60^\circ \text{ AD}) \\ \boldsymbol{D_{v30}}, (30^\circ \text{ AD}) \end{cases}. \tag{4}$$

in which, $\boldsymbol{D_{v30}}$ is for 30°-AD dual 3-ph PMSMs, known as the vector space decomposition matrix [18], is shown as

$$\boldsymbol{D_{v30}} = \frac{1}{3}\begin{bmatrix} 1 & \frac{\sqrt{3}}{2} & -\frac{1}{2} & -\frac{\sqrt{3}}{2} & -\frac{1}{2} & 0 \\ 0 & \frac{1}{2} & \frac{\sqrt{3}}{2} & \frac{1}{2} & -\frac{\sqrt{3}}{2} & -1 \\ 1 & -\frac{\sqrt{3}}{2} & -\frac{1}{2} & \frac{\sqrt{3}}{2} & -\frac{1}{2} & 0 \\ 0 & \frac{1}{2} & -\frac{\sqrt{3}}{2} & \frac{1}{2} & \frac{\sqrt{3}}{2} & -1 \\ 1 & 0 & 1 & 0 & 1 & 0 \\ 0 & 1 & 0 & 1 & 0 & 1 \end{bmatrix}; \tag{5}$$

$\boldsymbol{D_{v0,60}}$ is originally for 60°-AD dual 3-ph PMSMs [20] and expressed as

$$\boldsymbol{D_{v0,60}} = \frac{1}{3}\begin{bmatrix} 1 & \frac{1}{2} & -\frac{1}{2} & -1 & -\frac{1}{2} & \frac{1}{2} \\ 0 & \frac{\sqrt{3}}{2} & \frac{\sqrt{3}}{2} & 0 & -\frac{\sqrt{3}}{2} & -\frac{\sqrt{3}}{2} \\ 1 & -\frac{1}{2} & -\frac{1}{2} & 1 & -\frac{1}{2} & -\frac{1}{2} \\ 0 & \frac{\sqrt{3}}{2} & -\frac{\sqrt{3}}{2} & 0 & \frac{\sqrt{3}}{2} & -\frac{\sqrt{3}}{2} \\ 1 & 1 & 1 & 1 & 1 & 1 \\ 1 & -1 & 1 & -1 & 1 & -1 \end{bmatrix}. \tag{6}$$

However, for 0°-AD dual 3-ph PMSMs, a conversion is implemented to achieve an equivalent 60°-AD machine topology. A 0°-AD dual 3-ph PMSM with phase shifts of voltages and currents for Phase U, V, W can be viewed as a 60°-AD dual 3-ph PMSM, which is detailed in Fig. 2. Currents of Phase U, V, W in 0°-AD dual 3-ph PMSMs are converted to equivalent currents of the set U′V′W′ in the topology of the 60°-AD machines by

$$\begin{cases} i_{U'} = -i_W \\ i_{V'} = -i_U \\ i_{W'} = -i_V \end{cases}, \tag{7}$$

where $i_{U'}$, $i_{V'}$, $i_{W'}$ are equivalent currents of Phase U′, V′ and W′, respectively, as shown in the transformed 60°-AD topology after conversion. After current regulation, equivalent voltages

are generated, they are converted back to voltages for 0°-AD dual 3-ph PMSMs by

$$\begin{cases} u_U^* = -u_{V'}^* \\ u_V^* = -u_{W'}^* \\ u_W^* = -u_{U'}^* \end{cases} \tag{8}$$

in which, $u_{U'}^*$, $u_{V'}^*$, $u_{W'}^*$ are equivalent voltage references (60°-AD machine topology) in the control loop. Then, $\boldsymbol{D_{v0,60}}$ is then extended to 0°-AD dual 3-ph PMSMs and the decomposition of mutual inductances for 0°-AD dual 3-ph PMSMs is achieved indirectly.

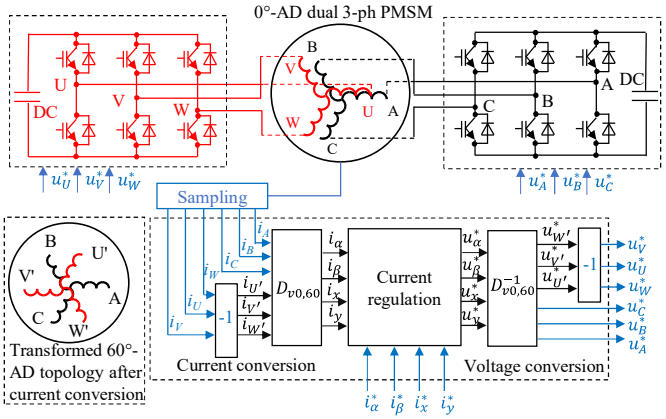

Fig. 2 Conversion of 0°-AD dual 3-ph PMSMs to 60°-AD machine topology in control loop.

Applying $\boldsymbol{D_v}$ to (1), voltages, currents, and flux linkages in three two-dimensional orthogonal subspaces (αβ, xy, and o_1o_2 subspaces) are generated and shown in (9).

$$\begin{cases} [u_\alpha \quad u_\beta \quad u_x \quad u_y \quad u_{o1} \quad u_{o2}]^{\mathrm{T}} = \boldsymbol{D_v u_s} \\ [i_\alpha \quad i_\beta \quad i_x \quad i_y \quad i_{o1} \quad i_{o2}]^{\mathrm{T}} = \boldsymbol{D_v i_s} \\ [\psi_\alpha \quad \psi_\beta \quad \psi_x \quad \psi_y \quad \psi_{o1} \quad \psi_{o2}]^{\mathrm{T}} = \boldsymbol{D_v \psi_s} \end{cases} \tag{9}$$

Since the projection of current vectors in o_1o_2 subspace is inherently zero, the o_1o_2 subspace is not taken into consideration. The generalized decomposition model derived from (9) is explained as

$$\begin{bmatrix} u_\alpha \\ u_\beta \\ u_x \\ u_y \end{bmatrix} = \begin{bmatrix} R_s & 0 & 0 & 0 \\ 0 & R_s & 0 & 0 \\ 0 & 0 & R_s & 0 \\ 0 & 0 & 0 & R_s \end{bmatrix} \begin{bmatrix} i_\alpha \\ i_\beta \\ i_x \\ i_y \end{bmatrix} + \begin{bmatrix} \dot{\psi}_\alpha \\ \dot{\psi}_\beta \\ \dot{\psi}_x \\ \dot{\psi}_y \end{bmatrix} \tag{10}$$

$$\begin{bmatrix} \psi_\alpha \\ \psi_\beta \\ \psi_x \\ \psi_y \end{bmatrix} = \begin{bmatrix} L_\sigma + 3M_1 & 0 & 0 & 0 \\ 0 & L_\sigma + 3M_1 & 0 & 0 \\ 0 & 0 & L_\sigma & 0 \\ 0 & 0 & 0 & L_\sigma \end{bmatrix} \begin{bmatrix} i_\alpha \\ i_\beta \\ i_x \\ i_y \end{bmatrix} + \begin{bmatrix} \cos(\theta_e) \\ \sin(\theta_e) \\ 0 \\ 0 \end{bmatrix} \psi_{fd}. \tag{11}$$

From (10) and (11), there are no coupling terms in αβ and xy subspaces.

III. Influences of Asymmetric Impedances on Generalized Decomposition Model

The generalized decomposition model in Section II is established on the premise of no asymmetric impedances. In this section, the research of asymmetric impedances affecting this generalized model is divided into three categories, which are asymmetric resistances, asymmetric self-inductances, and partially coupled mutual inductances. Then, according to the analytical model of asymmetric impedances, the compensation capability at a given DC link voltage is explained.

A. Asymmetric Resistances

Assuming the asymmetric resistance in each phase is ΔR_A, ΔR_B, ΔR_C, ΔR_U, ΔR_V and ΔR_W, respectively, $\boldsymbol{R_s}$ in (2) is changed as

$$\begin{aligned} \boldsymbol{R_s} = diag[&R_s + \Delta R_A \quad R_s + \Delta R_U \quad R_s + \Delta R_B \\ &R_s + \Delta R_V \quad R_s + \Delta R_C \quad R_s + \Delta R_W]. \end{aligned} \tag{12}$$

Then, the generalized decomposition model shown in (10) is modified as

$$\begin{bmatrix} u_\alpha \\ u_\beta \\ u_x \\ u_y \end{bmatrix} = \begin{bmatrix} R_s & 0 & 0 & 0 \\ 0 & R_s & 0 & 0 \\ 0 & 0 & R_s & 0 \\ 0 & 0 & 0 & R_s \end{bmatrix} \begin{bmatrix} i_\alpha \\ i_\beta \\ i_x \\ i_y \end{bmatrix} + \boldsymbol{R_{as}} \begin{bmatrix} i_\alpha \\ i_\beta \\ i_x \\ i_y \end{bmatrix} + \begin{bmatrix} \dot{\psi}_\alpha \\ \dot{\psi}_\beta \\ \dot{\psi}_x \\ \dot{\psi}_y \end{bmatrix}, \tag{13}$$

in which

$$\boldsymbol{R_{as}} = \begin{cases} \boldsymbol{R_{as0,60}} \ (0^\circ/60^\circ \text{ AD}) \\ \boldsymbol{R_{as30}} \ (30^\circ \text{ AD}) \end{cases}, \tag{14}$$

$$\boldsymbol{R_{as0,60}} = \begin{bmatrix} R_{0,60A1} & R_{0,60A3} & R_{0,60A5} & R_{0,60A4} \\ R_{0,60A3} & R_{0,60A2} & -R_{0,60A4} & R_{0,60A6} \\ R_{0,60A5} & -R_{0,60A4} & R_{0,60A1} & -R_{0,60A3} \\ R_{0,60A4} & R_{0,60A6} & -R_{0,60A3} & R_{0,60A2} \end{bmatrix}, \tag{15}$$

$$\begin{cases} R_{0,60A1} = \dfrac{\Delta R_A}{3} + \dfrac{\Delta R_B}{12} + \dfrac{\Delta R_C}{12} + \dfrac{\Delta R_U}{12} + \dfrac{\Delta R_V}{3} + \dfrac{\Delta R_W}{12} \\ R_{0,60A2} = \dfrac{\Delta R_B}{4} + \dfrac{\Delta R_C}{4} + \dfrac{\Delta R_U}{4} + \dfrac{\Delta R_W}{4} \\ R_{0,60A3} = \dfrac{\sqrt{3}(-\Delta R_B + \Delta R_C + \Delta R_U - \Delta R_W)}{12} \\ R_{0,60A4} = \dfrac{\sqrt{3}(\Delta R_B - \Delta R_C + \Delta R_U - \Delta R_W)}{12} \\ R_{0,60A5} = \dfrac{\Delta R_A}{3} + \dfrac{\Delta R_B}{12} + \dfrac{\Delta R_C}{12} - \dfrac{\Delta R_U}{12} - \dfrac{\Delta R_V}{3} - \dfrac{\Delta R_W}{12} \\ R_{0,60A6} = -\dfrac{\Delta R_B}{4} - \dfrac{\Delta R_C}{4} + \dfrac{\Delta R_U}{4} + \dfrac{\Delta R_W}{4} \end{cases}, \tag{16}$$

$$\boldsymbol{R_{as30}} = \begin{bmatrix} R_{30A1} & R_{30A3} & R_{30A5} & R_{30A4} \\ R_{30A3} & R_{30A2} & -R_{30A4} & R_{30A6} \\ R_{30A5} & -R_{30A4} & R_{30A1} & -R_{30A3} \\ R_{30A4} & R_{30A6} & -R_{30A3} & R_{30A2} \end{bmatrix}, \tag{17}$$

$$\begin{cases} R_{30A1} = \dfrac{\Delta R_A}{3} + \dfrac{\Delta R_B}{12} + \dfrac{\Delta R_C}{12} + \dfrac{\Delta R_U}{4} + \dfrac{\Delta R_V}{4} \\ R_{30A} = \dfrac{\Delta R_B}{4} + \dfrac{\Delta R_C}{4} + \dfrac{\Delta R_U}{12} + \dfrac{\Delta R_V}{12} + \dfrac{\Delta R_W}{3} \\ R_{30A3} = \dfrac{\sqrt{3}(-\Delta R_B + \Delta R_C + \Delta R_U - \Delta R_V)}{12} \\ R_{30A4} = \dfrac{\sqrt{3}(\Delta R_B - \Delta R_C + \Delta R_U - \Delta R_V)}{12} \\ R_{30A5} = \dfrac{\Delta R_A}{3} + \dfrac{\Delta R_B}{12} + \dfrac{\Delta R_C}{12} - \dfrac{\Delta R_U}{4} - \dfrac{\Delta R_V}{4} \\ R_{30A6} = -\dfrac{\Delta R_B}{4} - \dfrac{\Delta R_C}{4} + \dfrac{\Delta R_U}{12} + \dfrac{\Delta R_V}{12} + \dfrac{\Delta R_W}{3} \end{cases}. \quad (18)$$

From (14)-(18), $\boldsymbol{R_{as}}$ results in the coupling of αβ subspace and xy subspace, so that the two subspaces are not completely decoupled anymore. It is acknowledged that the fundamental components in i_α and i_β are the main contribution to torque generation. Therefore, the coupling of i_α and i_β into xy subspace could induce fundamental components in i_x and i_y without compensation. Then, cancelling them contributes to phase current balancing.

B. Asymmetric Self-inductances

Considering the asymmetric self-inductances, denoted by ΔL_A, ΔL_B, ΔL_C, ΔL_U, ΔL_V and ΔL_W, $\boldsymbol{L_s}$ in (2) is changed as

$$\begin{aligned} \boldsymbol{L_s} = L_\sigma \boldsymbol{I_6} + \begin{bmatrix} \Delta L_A & 0 & 0 & 0 & 0 & 0 \\ 0 & \Delta L_U & 0 & 0 & 0 & 0 \\ 0 & 0 & \Delta L_B & 0 & 0 & 0 \\ 0 & 0 & 0 & \Delta L_V & 0 & 0 \\ 0 & 0 & 0 & 0 & \Delta L_C & 0 \\ 0 & 0 & 0 & 0 & 0 & \Delta L_W \end{bmatrix} \\ + \begin{bmatrix} M_1 & M_{AU} & M_{AB} & M_{AV} & M_{AC} & M_{AW} \\ M_{AU} & M_1 & M_{BU} & M_{UV} & M_{CU} & M_{UW} \\ M_{AB} & M_{BU} & M_1 & M_{BV} & M_{BC} & M_{BW} \\ M_{AV} & M_{UV} & M_{BV} & M_1 & M_{CV} & M_{VW} \\ M_{AC} & M_{CU} & M_{BC} & M_{CV} & M_1 & M_{CW} \\ M_{AW} & M_{UW} & M_{BW} & M_{VW} & M_{CW} & M_1 \end{bmatrix}, \end{aligned} \quad (19)$$

where fully coupled mutual inductances are still assumed. Then, (11) is modified as

$$\begin{aligned} \begin{bmatrix} \psi_\alpha \\ \psi_\beta \\ \psi_x \\ \psi_y \end{bmatrix} = \begin{bmatrix} L_\sigma + 3M_1 & 0 & 0 & 0 \\ 0 & L_\sigma + 3M_1 & 0 & 0 \\ 0 & 0 & L_\sigma & 0 \\ 0 & 0 & 0 & L_\sigma \end{bmatrix} \begin{bmatrix} i_\alpha \\ i_\beta \\ i_x \\ i_y \end{bmatrix} \\ + \boldsymbol{L_{as}} \begin{bmatrix} i_\alpha \\ i_\beta \\ i_x \\ i_y \end{bmatrix} + \begin{bmatrix} \cos(\theta_e) \\ \sin(\theta_e) \\ 0 \\ 0 \end{bmatrix} \psi_{fd}, \end{aligned} \quad (20)$$

in which

$$\boldsymbol{L_{as}} = \begin{cases} \boldsymbol{L_{as0,60}} \ (0^\circ/60^\circ \text{ AD}) \\ \boldsymbol{L_{as30}} \ (30^\circ \text{ AD}) \end{cases}, \quad (21)$$

$$\boldsymbol{L_{as0,60}} = \begin{bmatrix} L_{0,60A1} & L_{0,60A3} & L_{0,60A5} & L_{0,60A4} \\ L_{0,60A3} & L_{0,60A2} & -L_{0,60A4} & L_{0,60A6} \\ L_{0,60A5} & -L_{0,60A4} & L_{0,60A1} & -L_{0,60A3} \\ L_{0,60A4} & L_{0,60A6} & -L_{0,60A3} & L_{0,60A2} \end{bmatrix}, \quad (22)$$

$$\begin{cases} L_{0,60A1} = \dfrac{\Delta L_A}{3} + \dfrac{\Delta L_B}{12} + \dfrac{\Delta L_C}{12} + \dfrac{\Delta L_U}{12} + \dfrac{\Delta L_V}{3} + \dfrac{\Delta L_W}{12} \\ L_{0,60A2} = \dfrac{\Delta L_B}{4} + \dfrac{\Delta L_C}{4} + \dfrac{\Delta L_U}{4} + \dfrac{\Delta L_W}{4} \\ L_{0,60A3} = \dfrac{\sqrt{3}(-\Delta L_B + \Delta L_C + \Delta L_U - \Delta L_W)}{12} \\ L_{0,60A4} = \dfrac{\sqrt{3}(\Delta L_B - \Delta L_C + \Delta L_U - \Delta L_W)}{12} \\ L_{0,60A5} = \dfrac{\Delta L_A}{3} + \dfrac{\Delta L_B}{12} + \dfrac{\Delta L_C}{12} - \dfrac{\Delta L_U}{12} - \dfrac{\Delta L_V}{3} - \dfrac{\Delta L_W}{12} \\ L_{0,60A6} = -\dfrac{\Delta L_B}{4} - \dfrac{\Delta L_C}{4} + \dfrac{\Delta L_U}{4} + \dfrac{\Delta L_W}{4} \end{cases}, \quad (23)$$

$$\boldsymbol{L_{as30}} = \begin{bmatrix} L_{30A1} & L_{30A3} & L_{30A5} & L_{30A4} \\ L_{30A3} & L_{30A2} & -L_{30A4} & L_{30A6} \\ L_{30A} & -L_{30A4} & L_{30A1} & -L_{30A3} \\ L_{30A4} & L_{30A6} & -L_{30A3} & L_{30A2} \end{bmatrix}, \quad (24)$$

$$\begin{cases} L_{30A1} = \dfrac{\Delta L_A}{3} + \dfrac{\Delta L_B}{12} + \dfrac{\Delta L_C}{12} + \dfrac{\Delta L_U}{4} + \dfrac{\Delta L_V}{4} \\ L_{30A2} = \dfrac{\Delta L_B}{4} + \dfrac{\Delta L_C}{4} + \dfrac{\Delta L_U}{12} + \dfrac{\Delta L_V}{12} + \dfrac{\Delta L_W}{3} \\ L_{30A3} = \dfrac{\sqrt{3}(-\Delta L_B + \Delta L_C + \Delta L_U - \Delta L_V)}{12} \\ L_{30A4} = \dfrac{\sqrt{3}(\Delta L_B - \Delta L_C + \Delta L_U - \Delta L_V)}{12} \\ L_{30A5} = \dfrac{\Delta L_A}{3} + \dfrac{\Delta L_B}{12} + \dfrac{\Delta L_C}{12} - \dfrac{\Delta L_U}{4} - \dfrac{\Delta L_V}{4} \\ L_{30A6} = -\dfrac{\Delta L_B}{4} - \dfrac{\Delta L_C}{4} + \dfrac{\Delta L_U}{12} + \dfrac{\Delta L_V}{12} + \dfrac{\Delta L_W}{3} \end{cases} \quad (25)$$

From (21)-(25), the influence of asymmetric self-inductances on the flux linkage equation is similar to that of asymmetric self-resistances on the voltage equation shown in (14)-(18). However, the influences appear in voltage equations eventually.

C. Partially Coupled Mutual Inductances

Given that mutual inductances M_{KL} $(K, L = A, B, C, U, V, W; K \neq L)$ coupling phases with the same spatial angle shift are the same, $\boldsymbol{L_s}$ in (2) is changed as (26). In (26), M_{30}, M_{60}, M_{90}, M_{120}, M_{150}, and M_{180} denote mutual inductances between phases with 30°, 60°, 90°, 120°, 150°, and 180° spatial angle shift, respectively. The third expression $M_{KL} = M_1 \cdot \cos(\theta_{KL})$ $(K, L = A, B, C, U, V, W; K \neq L)$ in (3) is not practical anymore, since mutual inductances are not fully coupled. Then, (11) is modified as (27).

In (27) and (28), for 30°-AD dual 3-ph PMSMs, the term L_4 in (27) results in the coupling of αβ subspace and xy subspace. The coupling of i_β into x-axis and the coupling of i_α into y-axis lead to additional fundamental flux linkages in xy subspace. The fundamental components in i_x and i_y are then excited

without compensation in xy subspace. For 60°-AD dual 3-ph PMSM topology, the mutual inductances between αβ and xy subspaces are cancelled.

$$\boldsymbol{L_s} = L_\sigma \boldsymbol{I_6} + \begin{cases} (0^\circ/60^\circ \text{ AD}) \\ \begin{bmatrix} M_1 & M_{60} & M_{120} & M_{180} & M_{120} & M_{60} \\ M_{60} & M_1 & M_{60} & M_{120} & M_{180} & M_{120} \\ M_{120} & M_{60} & M_1 & M_{60} & M_{120} & M_{180} \\ M_{180} & M_{120} & M_{60} & M_1 & M_{60} & M_{120} \\ M_{120} & M_{180} & M_{120} & M_{60} & M_1 & M_{60} \\ M_{60} & M_{120} & M_{180} & M_{120} & M_{60} & M_1 \end{bmatrix} \\ (30^\circ \text{ AD}) \\ \begin{bmatrix} M_1 & M_{30} & M_{120} & M_{150} & M_{120} & M_{90} \\ M_{30} & M_1 & M_{90} & M_{120} & M_{150} & M_{120} \\ M_{120} & M_{90} & M_1 & M_{30} & M_{120} & M_{150} \\ M_{150} & M_{120} & M_{30} & M_1 & M_{90} & M_{120} \\ M_{120} & M_{150} & M_{120} & M_{90} & M_1 & M_{30} \\ M_{90} & M_{120} & M_{150} & M_{120} & M_{30} & M_1 \end{bmatrix} \end{cases} \quad (26)$$

The winding layout of 60°-AD machines (Fig. 1) is symmetric spatially. In other words, the angle displacement between two adjacent phases is always 60°, resulting in three different values of mutual inductances (M_{60}, M_{120} and M_{180}). However, for 30°-AD machines, the angle displacement between two adjacent phases can be 30° or 90° (It means an asymmetric layout spatially) resulting in four different values of mutual inductances (M_{30}, M_{90}, M_{120} and M_{150}). The symmetric layout of 60°-AD machines benefits the cancellation of the mutual inductances between αβ and xy subspaces after the transform.

$$\begin{bmatrix} \psi_\alpha \\ \psi_\beta \\ \psi_x \\ \psi_y \end{bmatrix} = \begin{bmatrix} L_\sigma & 0 & 0 & 0 \\ 0 & L_\sigma & 0 & 0 \\ 0 & 0 & L_\sigma & 0 \\ 0 & 0 & 0 & L_\sigma \end{bmatrix} \begin{bmatrix} i_\alpha \\ i_\beta \\ i_x \\ i_y \end{bmatrix} + \begin{bmatrix} \cos(\theta_e) \\ \sin(\theta_e) \\ 0 \\ 0 \end{bmatrix} \psi_{fd} + \begin{cases} \begin{bmatrix} L_1 & 0 & 0 & 0 \\ 0 & L_1 & 0 & 0 \\ 0 & 0 & L_2 & 0 \\ 0 & 0 & 0 & L_2 \end{bmatrix} \begin{bmatrix} i_\alpha \\ i_\beta \\ i_x \\ i_y \end{bmatrix} (0^\circ/60^\circ \text{ AD}) \\ \begin{bmatrix} L_3 & 0 & 0 & L_4 \\ 0 & L_3 & L_4 & 0 \\ 0 & L_4 & L_5 & 0 \\ L_4 & 0 & 0 & L_5 \end{bmatrix} \begin{bmatrix} i_\alpha \\ i_\beta \\ i_x \\ i_y \end{bmatrix} (30^\circ \text{ AD}) \end{cases}, \quad (27)$$

in which

$$\begin{cases} L_1 = M_1 + M_{60} - M_{120} - M_{180} \\ L_2 = M_1 - M_{60} - M_{120} + M_{180} \\ L_3 = M_1 + \frac{\sqrt{3}}{2} M_{30} - M_{120} - \frac{\sqrt{3}}{2} M_{150} \\ L_4 = \frac{1}{2} M_{30} - M_{90} + \frac{1}{2} M_{150} \\ L_5 = M_1 - \frac{\sqrt{3}}{2} M_{30} - M_{120} + \frac{\sqrt{3}}{2} M_{150} \end{cases}. \quad (28)$$

D. Derivation of Compensation Capability

The compensation capability of impedance asymmetries can be derived through this model. At a certain torque or current requirement, whether the drive system can compensate the unbalanced currents caused by asymmetric impedances is acquired. From another aspect, in order to assure the achievement of compensation at a given condition of impedance asymmetries, the maximum torque value or current amplitudes can be estimated. If the machine operates beyond the estimated maximum value, the asymmetries fail to be balanced due to the limit of DC link voltage.

The model considering all asymmetric conditions can be summarized from (13), (20), and (27), as

$$\begin{bmatrix} u_\alpha \\ u_\beta \\ u_x \\ u_y \end{bmatrix} = \begin{bmatrix} R_s & 0 & 0 & 0 \\ 0 & R_s & 0 & 0 \\ 0 & 0 & R_s & 0 \\ 0 & 0 & 0 & R_s \end{bmatrix} \begin{bmatrix} i_\alpha \\ i_\beta \\ i_x \\ i_y \end{bmatrix} + \boldsymbol{R_{as}} \begin{bmatrix} i_\alpha \\ i_\beta \\ i_x \\ i_y \end{bmatrix} + \begin{bmatrix} \dot{\psi}_\alpha \\ \dot{\psi}_\beta \\ \dot{\psi}_x \\ \dot{\psi}_y \end{bmatrix}, \quad (29)$$

$$\begin{bmatrix} \psi_\alpha \\ \psi_\beta \\ \psi_x \\ \psi_y \end{bmatrix} = \begin{bmatrix} L_\sigma & 0 & 0 & 0 \\ 0 & L_\sigma & 0 & 0 \\ 0 & 0 & L_\sigma & 0 \\ 0 & 0 & 0 & L_\sigma \end{bmatrix} \begin{bmatrix} i_\alpha \\ i_\beta \\ i_x \\ i_y \end{bmatrix} + \begin{bmatrix} \cos(\theta_e) \\ \sin(\theta_e) \\ 0 \\ 0 \end{bmatrix} \psi_{fd} + \boldsymbol{L_{as}} \begin{bmatrix} i_\alpha \\ i_\beta \\ i_x \\ i_y \end{bmatrix} + \begin{cases} \begin{bmatrix} L_1 & 0 & 0 & 0 \\ 0 & L_1 & 0 & 0 \\ 0 & 0 & L_2 & 0 \\ 0 & 0 & 0 & L_2 \end{bmatrix} \begin{bmatrix} i_\alpha \\ i_\beta \\ i_x \\ i_y \end{bmatrix} (0^\circ/60^\circ \text{ AD}) \\ \begin{bmatrix} L_3 & 0 & 0 & L_4 \\ 0 & L_3 & L_4 & 0 \\ 0 & L_4 & L_5 & 0 \\ L_4 & 0 & 0 & L_5 \end{bmatrix} \begin{bmatrix} i_\alpha \\ i_\beta \\ i_x \\ i_y \end{bmatrix} (30^\circ \text{ AD}) \end{cases}. \quad (30)$$

Conventionally, the voltages in two subspaces are transformed back to phase voltages by inverse VSD decoupling matrix and then 3-ph SVPWM is conducted in two individual sets of 3-ph systems, shown in Fig. 3 [19], [36]. Then, the voltages in αβ reference frames in two sets of 3-ph systems can be expressed as

$$\begin{cases} u_{\alpha1} = u_\alpha + u_x \\ u_{\beta1} = u_\beta - u_y \\ u_{\alpha2} = \frac{1}{2} u_\alpha + \frac{\sqrt{3}}{2} u_\beta - \frac{1}{2} u_x + \frac{\sqrt{3}}{2} u_y \\ u_{\beta2} = -\frac{\sqrt{3}}{2} u_\alpha + \frac{1}{2} u_\beta + \frac{\sqrt{3}}{2} u_x + \frac{1}{2} u_y \end{cases} (0^\circ/60^\circ \text{ AD}) \quad (31)$$

$$\begin{cases} u_{\alpha1} = u_\alpha + u_x \\ u_{\beta1} = u_\beta - u_y \\ u_{\alpha2} = \frac{\sqrt{3}}{2} u_\alpha + \frac{1}{2} u_\beta - \frac{\sqrt{3}}{2} u_x + \frac{1}{2} u_y \\ u_{\beta2} = -\frac{1}{2} u_\alpha + \frac{\sqrt{3}}{2} u_\beta + \frac{1}{2} u_x + \frac{\sqrt{3}}{2} u_y \end{cases} (30^\circ \text{ AD}) \quad (32)$$

in which $u_{\alpha1}$, $u_{\beta1}$ and $u_{\alpha2}$, $u_{\beta2}$ denotes voltages in αβ reference frame of two sets of windings, respectively. Then, the switching sequence S_A, S_B, S_C and S_U, S_V, S_W are generated

separately by the 3-ph SVPWM technique. It is acknowledged that the modulation in two sets should be within the linear range, shown as

$$\begin{cases} \sqrt{u_{\alpha1}^2 + u_{\beta1}^2} \le \dfrac{\sqrt{3}}{3} \cdot V_{dc} \\ \sqrt{u_{\alpha2}^2 + u_{\beta2}^2} \le \dfrac{\sqrt{3}}{3} \cdot V_{dc} \end{cases}. \tag{33}$$

Assuming that phase currents are well regulated and balanced, the currents in two subspaces can be presented as

$$\begin{bmatrix} i_\alpha \\ i_\beta \\ i_x \\ i_y \end{bmatrix} = \begin{bmatrix} i_d\cos(\theta_e) - i_q\sin(\theta_e) \\ i_d\sin(\theta_e) + i_q\cos(\theta_e) \\ 0 \\ 0 \end{bmatrix}, \tag{34}$$

in which, i_d and i_q denote currents on d-axis and q-axis, respectively. Substitute (29), (30), (31), (32), and (34) into (33) at a given electrical angular speed, (33) should be satisfied at given i_d and i_q with $\theta_e \in [0, 2\pi]$. Furthermore, at a given i_d or $i_d = 0$, the maximum amplitude of i_q can be derived. Then, the maximum torque value restricted by the DC link voltage can be estimated, while assuring the compensation of given impedance asymmetries.

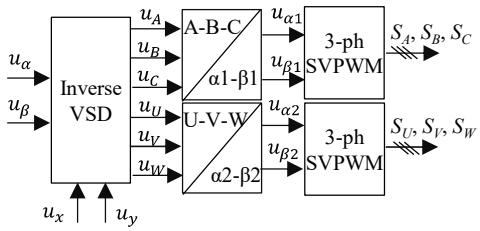

Fig. 3 SVPWM for dual 3-ph machines.

IV. Compensation Strategy for Asymmetric Impedances and System Harmonics

In this section, a compensation strategy to balance phase currents under impedance asymmetries is explained. A 30°-AD dual 3-ph PMSM is used as an example to illustrate the compensation strategy. Of note, PIR (PI+ resonant) controllers are implemented to suppress unbalanced fundamental components and the 5th, 7th harmonic currents caused by system harmonics, i.e. distorted EMF and inverter nonlinearities. The topology of the compensation strategy is explained in Fig. 4. The testing 30°-AD dual 3-ph PMSM is operating at a generator mode.

For the compensation of system harmonics, the 5th and 7th order current harmonics decoupled in xy subspace [18] are converted into the 6th order current harmonic in the rotating reference frame of xy subspace after the implementation of Park transform in xy subspace. In Fig. 4, the Park transform is shown as

$$\begin{bmatrix} i_d \\ i_q \\ i_{xr} \\ i_{yr} \end{bmatrix} = \begin{bmatrix} \cos\theta_e & \sin\theta_e & 0 & 0 \\ -\sin\theta_e & \cos\theta_e & 0 & 0 \\ 0 & 0 & -\cos(\theta_e) & \sin(\theta_e) \\ 0 & 0 & \sin(\theta_e) & \cos(\theta_e) \end{bmatrix} \begin{bmatrix} i_\alpha \\ i_\beta \\ i_x \\ i_y \end{bmatrix}, \tag{35}$$

in which, i_{xr}, i_{yr} denote i_x, i_y after the Park transform. Similarly, u_{xr}, u_{yr} denote u_x, u_y after the Park transform in xy subspace. Meanwhile, u_d and u_q denote voltages on d-axis and q-axis, respectively.

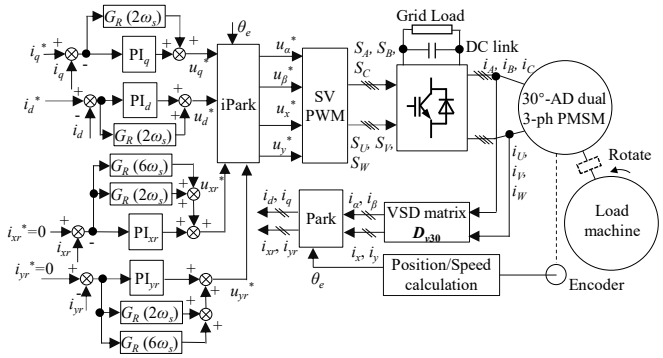

Fig. 4 Block diagram of compensation strategy for asymmetric impedances and harmonics.

From the previous analysis, asymmetric impedances lead to additional fundamental components in two subspaces due to the coupling terms shown in Section III. After Park transform, there would be the additional 2nd order harmonics in both subspaces. Therefore, resonant controllers are implemented to suppress the 2nd harmonic in αβ subspace and the 2nd, 6th harmonics in xy subspace. The advantage of resonant controllers is to provide a large gain at the required frequencies, thereby achieving the harmonic compensation performance. The transfer function of the resonant controller is

$$G_R(s) = \frac{K_r s}{s^2 + \omega_c s + (h\omega_s)^2}, \tag{36}$$

where K_r denotes the resonant gain; ω_c, ω_s denote cut-off frequency and fundamental frequency, respectively. ω_c determines the gain at resonant frequency and bandwidth. The Bode diagram of ω_c with different values at the condition of $\omega_s = 16.76$ rad/s, h=2, K_r=2750 is shown in Fig. 5. A small ω_c leads to a large gain and a small bandwidth around the resonant frequency. Details of parameter tuning approaches and performances can be seen in [32], [35]-[36]. In summary, the design of PIR controllers shown in Fig. 4 assures a good suppression performance of system harmonics and impedance asymmetries.

V. Experimental Validation of Compensation Strategy

In this section, the experimental performance with the compensation strategy is tested under different asymmetric conditions deliberately created by series connections of a resistor or an inductor. The purpose of the series connections of a resistor or an inductor is to create a relatively large asymmetric impedance, thereby showing the influences of asymmetric impedance and the effectiveness of the compensation strategy more apparently. A fractional-slot 42/32 (slot/pole) 30°-AD dual 3-ph PMSM with partially coupled mutual inductances and sinusoidal back-emf is tested. This test rig shown in Fig. 6 is constructed to test control strategies for direct-drive wind power applications operating at low speeds.

The 30°-AD dual 3-ph PMSM is operating at the generator mode with a fixed speed provided by a load PMSM machine. The DC link voltage is set to 250V and dSPACE is used to conduct the whole algorithm. The parameters of this PMSM are shown in Table I. Substituting mutual inductance values shown in Table I into (28), it converts into

$$\begin{cases} L_3 = 17 + 2.13\sqrt{3}\ (\text{mH}) \\ L_4 = 0.56\ (\text{mH}) \\ L_5 = 17 - 2.13\sqrt{3}\ (\text{mH}) \end{cases}. \tag{37}$$

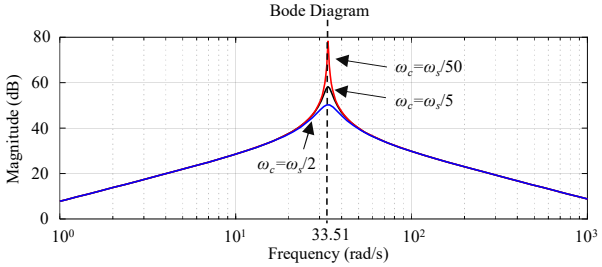

Fig. 5 Bode diagram of $G_R(s)$ with $\omega_c = \omega_s/2$, $\omega_s/5$, $\omega_s/50$, respectively, with $\omega_s = 16.76$ rad/s and h=2.

Fig. 6 Test rig (left: load machine; right: dual 3-ph PMSM).

TABLE I
PARAMETERS OF FRACTIONAL-SLOT 42/32 (SLOT/POLE) 30°-AD DUAL 3-PH PMSM

Parameters	Value
Rated power	3.7 kW
Rated speed	170 r/min
Rated torque	209 Nm
Stator resistance	3.3 Ω
PM Flux	1.03 Wb
Number of pole pairs	16
Self-inductance M_1	17.21 mH
Mutual inductance M_{30}, M_{90}, M_{120}, M_{150}	2.73, 0.04, 0.21, -1.53 mH

As illustrated previously, apparent asymmetric resistances or inductances are introduced in this test machine by a 3.3Ω resistor or 20mH inductor connected to Phase A in series. For the condition of a 3.3Ω resistor connected to Phase A in series, (17) can be simplified as

$$\boldsymbol{R_{as30}} = \begin{bmatrix} \frac{\Delta R_A}{3} & 0 & \frac{\Delta R_A}{3} & 0 \\ 0 & 0 & 0 & 0 \\ \frac{\Delta R_A}{3} & 0 & \frac{\Delta R_A}{3} & 0 \\ 0 & 0 & 0 & 0 \end{bmatrix}, \tag{38}$$

in which ΔR_A =3.3Ω. It is clear that the term $\Delta R_A/3$ causes coupling of i_α into x-axis. Meanwhile, the 20mH inductor connected to Phase A in series results in a similar effect in the flux linkage equation. (24) can be simplified as

$$\boldsymbol{L_{as30}} = \begin{bmatrix} \frac{\Delta L_A}{3} & 0 & \frac{\Delta L_A}{3} & 0 \\ 0 & 0 & 0 & 0 \\ \frac{\Delta L_A}{3} & 0 & \frac{\Delta L_A}{3} & 0 \\ 0 & 0 & 0 & 0 \end{bmatrix}, \tag{39}$$

in which ΔL_A =20mH. Then, a fundamental current in i_x is expected as well through the term $\Delta L_A/3$, if there is no compensation in xy subspace.

To show the influences of the asymmetric impedances and to highlight the importance of the compensation strategy, the experiment of the control strategy whose control diagram is illustrated in Fig. 7 is conducted firstly. Compared with Fig. 4, $u_x^* = 0$, $u_y^* = 0$ are set in Fig. 7, which means no compensation regarding asymmetric impedances or harmonics in xy subspace. Meanwhile, only PI regulators in αβ subspace are remained to regulate the DC components in the d-q reference frame, thereby controlling the electromagnetic torque. This control strategy can offer a basic control of dual 3-ph machines. On the other hand, the analysis of influences of asymmetric impedances is validated through this control strategy.

Setting $i_d^* = 0$, $i_q^* = -3$A and the speed of 20 r/min, the experimental results of the control strategies illustrated in Fig. 7 (without compensation) and Fig. 4 (with compensation) are compared in Fig. 8 with the original test PMSM in the left column, an additional series 3.3Ω resistor in Phase A in the middle column and an additional 20mH inductor in the right column. The parameters of the PI controller are mainly determined according to [37] by optimizing the damping factor of the control system, while the gain of the resonant controller is set as the same as the integrator gain of PI controllers [36], [38]. Then, the PIR controller parameters are listed as K_p=45, K_i=2750 for i_d and i_q PI controllers; K_p=12, K_i=2750 for i_{xr} and i_{yr} PI controllers; K_r=2750, $\omega_c = \omega_s/50$ for all resonant controllers.

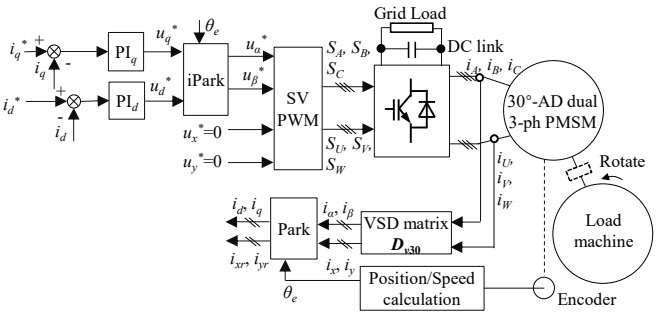

Fig. 7 Block diagram of control strategy without compensation for asymmetric impedances and harmonics.

The waveforms of phase currents and corresponding spectrum analysis of i_A, i_U are presented in Fig. 8(a) and (b), respectively. For the results without compensation in the original test PMSM (left), there are the 5th and 7th order harmonics caused by inverter nonlinearities and an unbalanced fundamental component between i_A and i_U. On the other hand, the series 3.3Ω resistor in Phase A (middle in Fig. 8(a) and (b)) leads to a large imbalance between the fundamental

components in i_A and i_U for the control strategy without compensation. Meanwhile, the imbalance led by the series 20mH inductor (right in Fig. 8(a) and (b)) is not that large. After compensation, the fundamental components in i_A and i_U are balanced and the 5th and 7th order harmonics are suppressed to nearly zero for all three conditions. Then, the effectiveness of phase current balancing is testified.

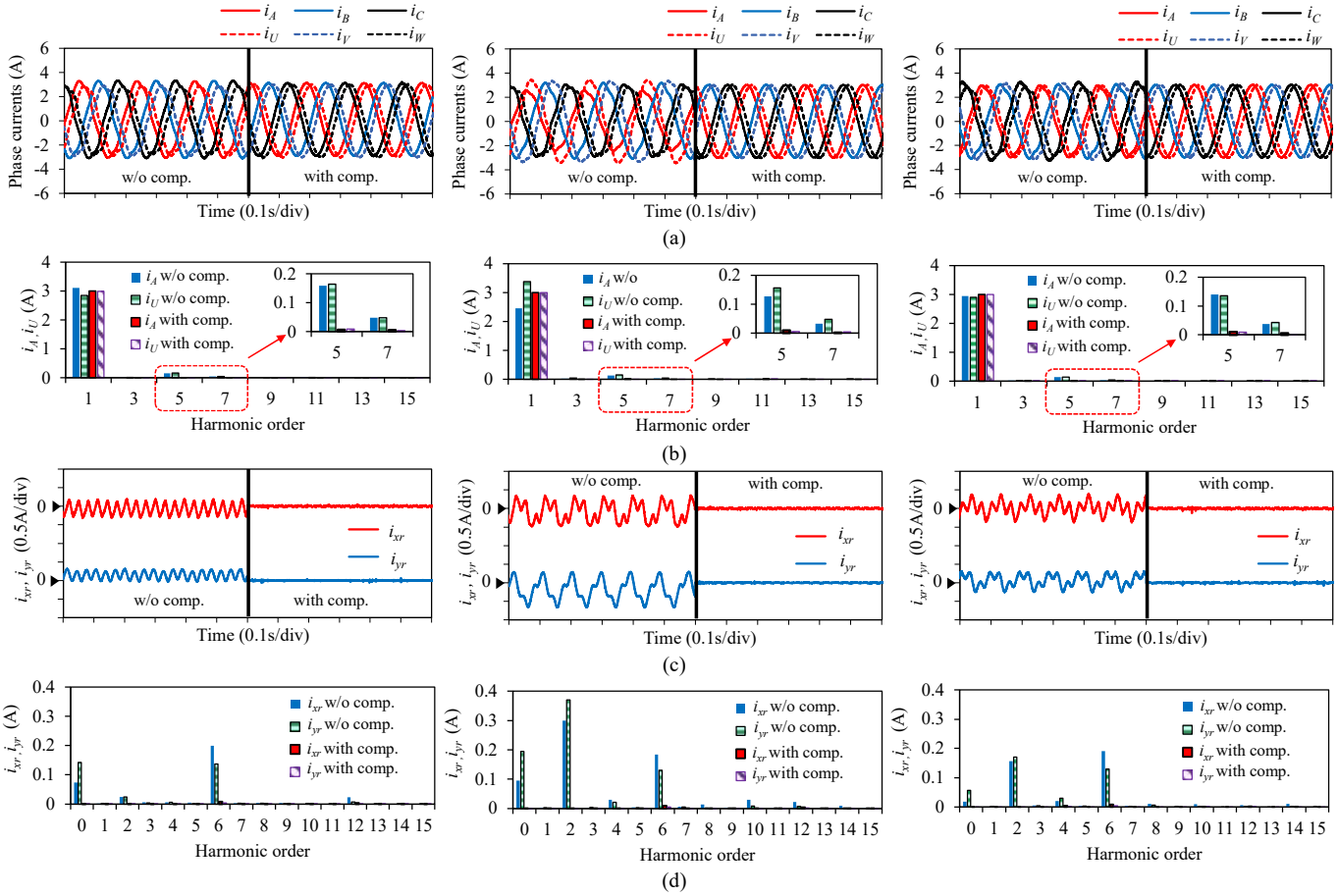

Fig. 8 Experimental comparison of control strategies illustrated in Fig. 7 (without compensation) and Fig. 4 (with compensation) under three different asymmetric conditions, original test PMSM (left), a series 3.3Ω resistor in Phase A (middle) and a series 20mH inductor in Phase A (right). (a) Waveforms of phase currents; (b) Spectrum analysis of currents in Phase A and U; (c) Waveforms of rotating currents in xy subspace; (d) Spectrum analysis of rotating currents in xy subspace.

Fig. 8(c) and (d) show rotating current waveforms of currents in xy subspace (i_{xr}, i_{yr}) and spectrum analysis under three conditions, respectively. For the original test PMSM without compensation for asymmetric impedances and harmonics (left), the DC component and 6th harmonics appear in i_{xr} and i_{yr}. On the other hand, the series 3.3Ω resistor in Phase A (middle) leads to an additional large DC component, 2nd harmonics in i_{xr} and i_{yr}. Similarly, the series 20mH inductor in Phase A results in a relatively small DC component and 2nd harmonics in i_{xr} and i_{yr}, since the value of the additional 20mH inductor is in a small order of magnitude. After compensation, the fundamental component, 2nd and 6th harmonics are significantly suppressed to nearly zero by the compensation strategy functioned in xy subspace.

Fig. 9 presents the difference of the fundamental components between i_A and i_U for the control strategies illustrated in Fig. 7 (without compensation) and Fig. 4 (with compensation) under different speeds with i_q=-3A and different loads (i_q) at the speed of 20 r/min, with a series 3.3Ω resistor in Phase A. The compensation strategy can offer a good phase current balancing performance at different speeds and loads.

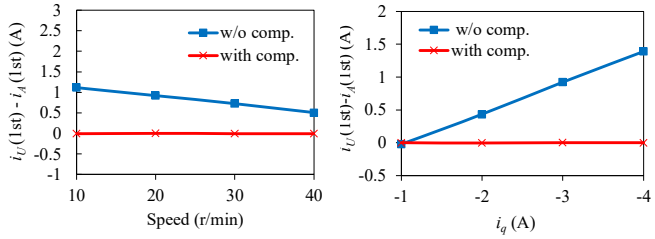

Fig. 9 Difference between Phase A and Phase U currents concerning fundamental component under the condition of a series 3.3Ω resistor in Phase A. (a) Different speeds at i_q= -3A. (b) Different i_q at the speed of 20 r/min.

With a series 3.3Ω resistor in Phase A, the dynamic performance of torque response for the compensation strategy (Fig. 4) with i_q changing from -1A to -3A at the speed of 20 r/min is shown in Fig. 10. Fig. 11 illustrates the dynamic performance of speed response for the compensation strategy (Fig. 4) with speed changing from 10 to 30 r/min at i_q=-3A under the condition of a series 3.3Ω resistor in Phase A. From Fig. 11(b), phase currents experience a smooth transient.

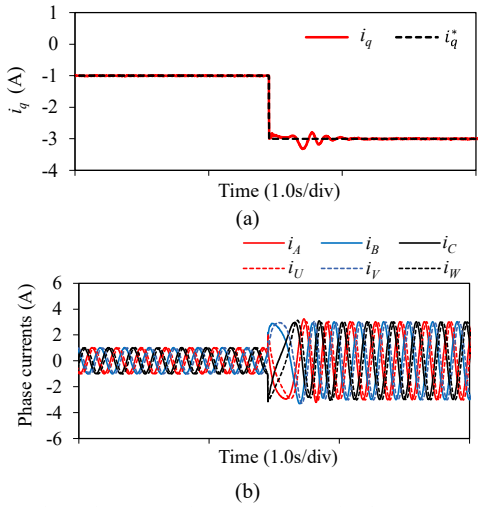

Fig. 10 Dynamic performance of torque response for the compensation strategy with q-axis current changing from -1A to -3A under the condition of a series 3.3Ω resistor in Phase A. (a) q-axis current. (b) Phase currents.

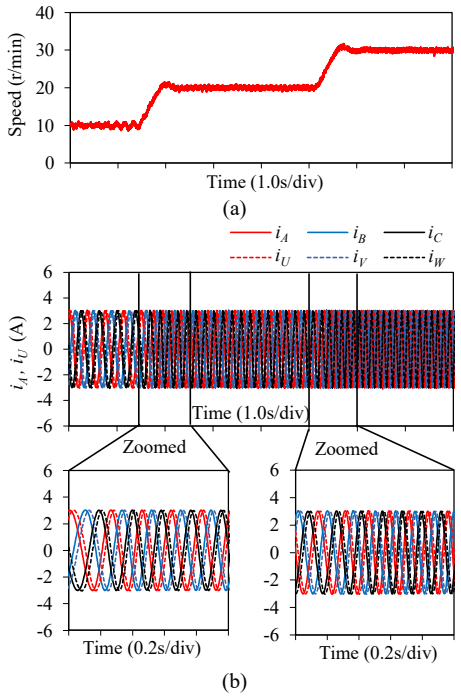

Fig. 11 Dynamic performance of speed response for the compensation strategy with speed changing from 10 to 30 r/min under the condition of a series 3.3Ω resistor in Phase A. (a) Speed. (b) Phase currents.

VI. Simulation Validation of Generalized Decomposition Model

A. Validation of Model Considering Impedance Asymmetries and Practice of Compensation Capability Analysis

To validate the model considering impedance asymmetries, a simulation platform using the same parameters as the experimental results is established. In the simulation platform, the ideal machine and the ideal inverter are built. In the simulation, The PIR controllers in αβ subspace are implemented to assure the control performance of currents on d-axis and q-axis, while no control is allocated in xy subspace. Setting $i_d^* = 0$, $i_q^* = -3\text{A}$, $u_x^* = 0$, $u_y^* = 0$ and the speed of 20 r/min, the model is tested under three conditions, partially coupled mutual inductances, fully coupled mutual inductances and a series 3.3Ω resistor in Phase A, fully coupled mutual inductances and a series 20mH inductor in Phase A, respectively. The currents in xy subspace are shown in Fig. 12.

Under the condition of partially coupled mutual inductances, the voltage-current equation on x-axis and y-axis in (29) can be rewritten as

$$\begin{cases} u_x = R_s \cdot i_x + L_4 \cdot \dfrac{di_\beta}{dt} + (L_5 + L_\sigma) \cdot \dfrac{di_x}{dt} \\ u_y = R_s \cdot i_y + L_4 \cdot \dfrac{di_\alpha}{dt} + (L_5 + L_\sigma) \cdot \dfrac{di_y}{dt} \end{cases}. \tag{40}$$

Substitute $i_d = 0$, $i_q = -3\text{A}$ and $u_x = u_y = 0$ into (40), the amplitudes of i_x and i_y are the same, which are 0.017A. It is calculated from Fig. 12(a) that the amplitudes of fundamental components of i_x and i_y are 0.015A and 0.017A, respectively. Then, the model regarding mutual inductances is verified.

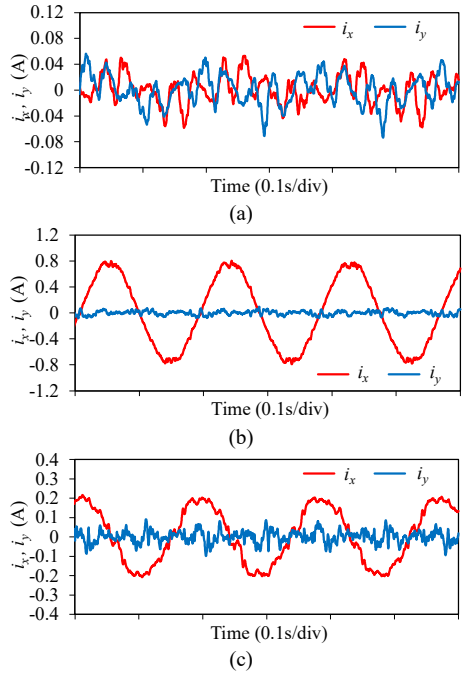

Fig. 12 Simulation result of current in xy subspace. (a) Partially coupled mutual inductances. (b) Fully coupled mutual inductances and a series 3.3Ω resistor in Phase A. (c) Fully coupled mutual inductances and a series 20mH inductor in Phase A.

Under the condition of fully coupled mutual inductances and a series 3.3Ω resistor in Phase A, the voltage-current equation on x-axis in (29) can be rewritten as

$$u_x = \frac{\Delta R_A}{3} \cdot i_\alpha + (\frac{\Delta R_A}{3} + R_s) \cdot i_x + L_\sigma \frac{di_x}{dt}. \tag{41}$$

The amplitude of i_x can be derived, which is 0.75A, confirmed with the amplitude of i_x in Fig. 12(b) (around 0.75A).

Under the condition of fully coupled mutual inductances and a series 20mH inductor in Phase A, the voltage-current equation on x-axis in (29) can be rewritten as

$$u_x = R_s \cdot i_x + \frac{\Delta L_A}{3} \cdot \frac{di_\alpha}{dt} + (\frac{\Delta L_A}{3} + L_\sigma) \cdot \frac{di_x}{dt}. \tag{42}$$

The amplitude of i_x can be calculated as 0.20A which is nearly the same as the amplitude of i_x in Fig. 12(c). Then, the model considering impedance asymmetries is validated quantitatively in this simulation.

Furthermore, an example of the compensation capability analysis under the condition of a series 3.3Ω resistor in Phase A at the speed of 20 r/min is explained. Substitute (34) with $i_d = 0$ and ideal machine parameters into (40) and (32), the boundary conditions in (33) can be plotted as Fig. 13 which shows that the system has the compensation capability regarding the series 3.3Ω resistor in Phase A, when the q-axis current is between -29.8A (lower limit) and 19.1A (upper limit). If the q-axis current is out of this range, the drive system cannot compensate the series 3.3Ω resistor in Phase A, restricted by the DC link voltage. Then, the boundary is tested in simulation. In Fig. 14, i_q=-29.8A is set and currents are well regulated and balanced, as shown in Fig. 14(a). From Fig. 14(b), the duty cycles are close to the saturation limit, validating the boundary described in Fig. 13. When i_q is out of the compensation area, as set to -32A shown in Fig. 15, the duty cycles are saturated and the compensation performance of unbalanced phase currents are affected.

Following the same rules, the lower and upper limits of q-axis currents can be derived at different speeds, shown in Fig. 16. Since the speed determines EMF and voltage drops on inductances, the compensation area is affected.

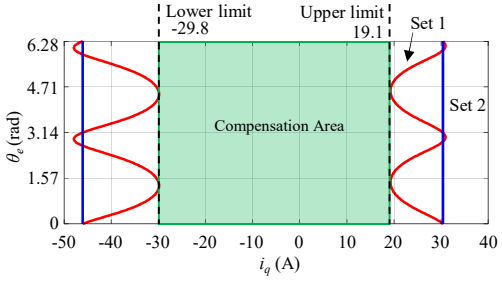

Fig. 13 Compensation capability under the condition of a series 3.3Ω resistor in Phase A at the speed of 20 r/min.

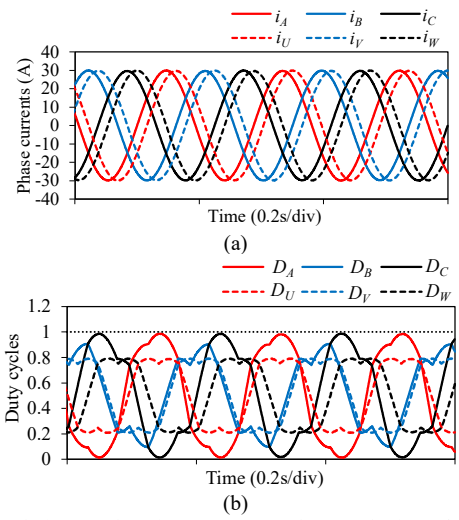

Fig. 14 Simulation results of i_q= -29.8A at the speed of 20 r/min under the condition of a series 3.3Ω resistor in Phase A. (a) Phase currents. (b) Duty cycle of each phase.

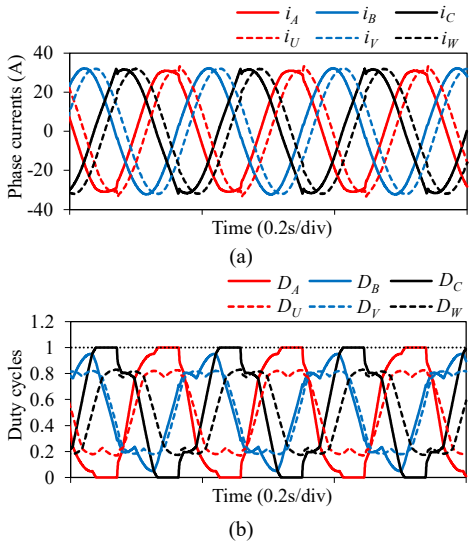

Fig. 15 Simulation results of i_q= -32A at the speed of 20 r/min under the condition of a series 3.3Ω resistor in Phase A. (a) Phase currents. (b) Duty cycle of each phase.

B. *Validation of Conversion of 0°-AD Dual 3-ph PMSMs to 60°-AD Machine Topology in Control Loop*

In this part, the conversion of 0°-AD dual 3-ph PMSM to 60°-AD machine topology in the control loop described in Fig. 2 is validated in simulation. The 0°-AD dual 3-ph PMSM with fully coupled mutual inductances is built in simulation with the parameters listed in Table I. The DC link voltage is set to 250V as well. The machine operates with PI current controllers in αβ subspace and $i_d^* = 0$, $i_q^* = -3$A, rotating at the speed of 20 r/min. The conversion performance is shown in Fig. 17. The currents sampled from 0°-AD dual 3-ph PMSMs in Fig. 17(a) is converted to equivalent current in 60°-AD dual 3-ph PMSMs shown in Fig. 17(b). The phase voltages generated from current controllers are shown in Fig. 17(c), which are then converted back to phase voltages in 0°-AD dual 3-ph PMSM.

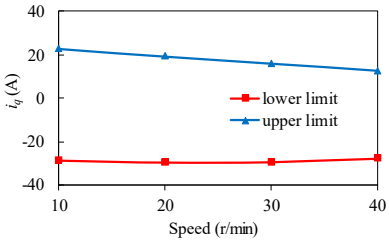

Fig. 16 Lower and upper limits of q-axis currents under the condition of a series 3.3Ω resistor in Phase A at different speeds.

VII. Conclusion

In this paper, the conversion of currents and voltages makes 0°-AD dual 3-ph PMSMs controlled in the equivalent machine model of 60°-AD dual 3-ph PMSMs. Then, a generalized decomposition model of 0°, 30°, and 60°-AD dual 3-ph PMSMs is formed, which solves the coupling of mutual inductances between phases from two sets, respectively, which are the barrier for two-set separate modelling.

It is noted that asymmetric impedances commonly existing in drive applications of dual 3-ph PMSMs cause unbalanced phase currents and can be well regulated in the generalized

decomposition model. Then, the generalized decomposition model is optimized considering impedance asymmetries. Through this model, the compensation capability of impedance asymmetries restricted by DC link voltage is derived. It indicates whether the drive system has the capability to fully compensate the impedance asymmetries at a given torque or current requirement.

Furthermore, the compensation strategy using PIR controllers can balance phase currents caused by asymmetric impedances effectively. The experimental results validate the decomposition model and the phase current balancing performance of compensation strategy. Additionally, complementary simulation results proof the developed model and the conversion of 0°-AD dual 3-ph PMSMs.

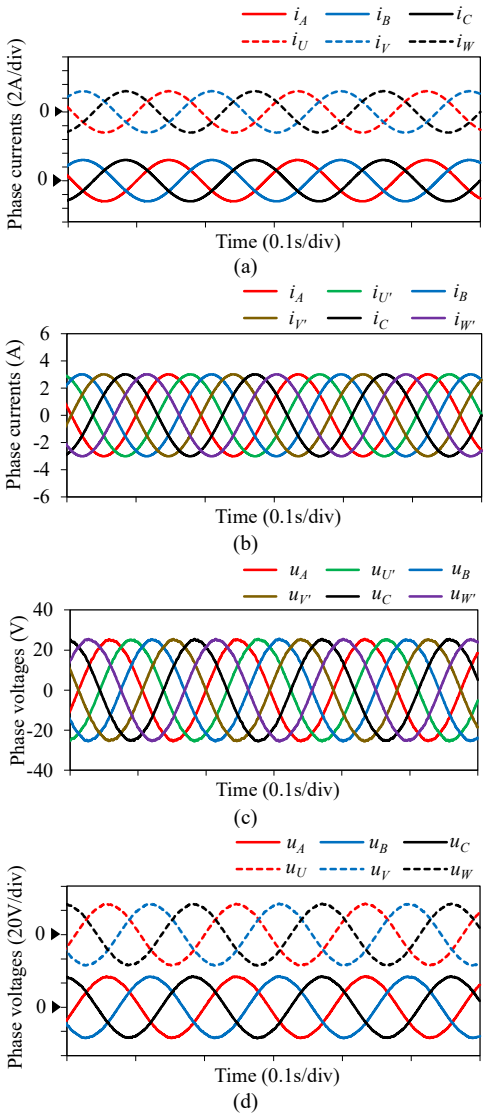

Fig. 17 Simulation results of conversion of 0°-AD dual 3-ph PMSMs to 60°-AD machine topology with reference to Fig. 2. (a) Phase currents in 0°-AD dual 3-ph PMSMs. (b) Phase currents in 60°-AD machine topology in control loop. (c) Phase voltages in 60°-AD machine topology in control loop. (d) Phase voltages of 0°-AD dual 3-ph PMSMs.

REFERENCES

[1] E. Levi, "Multiphase electric machines for variable-speed applications," *IEEE Trans. Ind. Electron.*, vol. 55, no. 5, pp. 1893–1909, May 2008.

[2] S. Hu, Z. Liang, W. Zhang, and X. He, "Research on the integration of hybrid energy storage system and dual three-phase PMSM drive in EV," *IEEE Trans. Ind. Electron.*, vol. 65, no. 8, pp. 6602–6611, Aug. 2018.

[3] J. Nerg, M. Rilla, V. Ruuskanen, J. Pyrhonen, and S. Ruotsalainen, "Direct-driven interior magnet permanent-magnet synchronous motors for a full electric sports car," *IEEE Trans. Ind. Electron.*, vol. 61, no. 8, pp. 4286–4294, Aug. 2014.

[4] E. Levi, "Advances in converter control and innovative exploitation of additional degrees of freedom for multiphase machines," *IEEE Trans. Ind. Electron.*, vol. 63, no. 1, pp. 433–448, Jan. 2016.

[5] P. Zheng, F. Wu, Y. Lei, Y. Sui, and B. Yu, "Investigation of a novel 24-slot/14-pole six-phase fault-tolerant modular permanent-magnet in wheel motor for electric vehicles," *Energies*, vol. 6, no. 10, pp. 4980– 5002, Sep. 2013.

[6] P. L. Xu, J. H. Feng, S. Y. Guo, S. Z. Feng, W. Q. Chu, Y. Ren, and Z. Q. Zhu, "Analysis of dual three-phase permanent magnet synchronous machines with different angle displacements," *IEEE Trans. Ind. Electron.*, vol. 65, no. 3, pp. 1941-1954, Mar. 2018.

[7] M. Barcaro, N. Bianchi, and F. Magnussen, "Analysis and tests of a dual three-phase 12-slot 10-pole permanent-magnet motor," *IEEE Trans. Ind. Appl.*, vol. 46, no. 6, pp. 2355-2362, Nov.-Dec. 2010.

[8] M. Zabaleta, E. Levi, and M. Jones, "A novel synthetic loading method for multiple three-phase winding electric machines," *IEEE Trans. Energy Convers.*, vol. 34, no. 1, pp. 70-78, Mar. 2019.

[9] A. S. Abdel-Khalik, S. Ahmed, and A. M. Massoud, "Low space harmonics cancelation in double-layer fractional slot winding using dual multiphase winding," *IEEE Trans. Magn.*, vol. 51, no. 5, pp. 1-10, May 2015.

[10] Y. Li, Z. Zhu, X. Wu, A. S. Thomas and Z. Wu, "Comparative study of modular dual 3-phase permanent magnet machines with overlapping/non-overlapping windings," *IEEE Trans. Ind. Appl.*, vol. 55, no. 4, pp. 3566-3576, Jul.-Aug. 2019.

[11] Y. X. Li, Z. Q. Zhu, A. S. Thomas, Z. Y. Wu and X. M. Wu, "Novel modular fractional slot permanent magnet machines with redundant teeth," *IEEE Trans. Magn.*, vol. 55, no. 9, pp. 1-10, Sep. 2019.

[12] M. Barcaro, N. Bianchi, and F. Magnussen, "Six-phase supply feasibility using a PM fractional-slot dual winding machine," *IEEE Trans. Ind. Appl.*, vol. 47, no. 5, pp. 2042-2050, Sep.-Oct. 2011.

[13] H. Dhulipati, S. Mukundan, W. Li, J. Tjong and N. C. Kar, "Investigation of phase angle displacements in six-phase PMSM with concentrated windings for reduced MMF harmonics," in *Proc. Int. Conf. Elect. Mach. Syst.*, 2018, pp. 308-313.

[14] A. Matyas, G. Aroquiadassou, C. Marţis, A. Mpanda-Mabwe, and K. Biro, "Design of six-phase synchronous and induction machines for EPS," in *Proc. Int. Conf. Elect. Mach.*, 2010, pp. 1-6.

[15] G. K. Singh, K. Nam, and S. K. Lim, "A simple indirect field-oriented control scheme for multiphase induction machine," *IEEE Trans. Ind. Electron.*, vol. 52, no. 4, pp. 1177–1184, Aug. 2005.

[16] Y. He, Y. Wang, J. Wu, Y. Feng, and J. Liu, "A simple current sharing scheme for dual three-phase permanent-magnet synchronous motor drives," in *Proc. Annu. IEEE Appl. Power Electron. Conf. Expo.*, 2010, pp. 1093–1096.

[17] R. O. C. Lyra, and T. A. Lipo, "Torque density improvement in a six-phase induction motor with third harmonic current injection," *IEEE Trans. Ind. Appl.*, vol. 38, no. 5, pp. 1351-1360, Sep./Oct. 2002.

[18] Y. Zhao, and T. A. Lipo, "Space vector PWM control of dual three-phase induction machine using vector space decomposition," *IEEE Trans. Ind. Appl.*, vol. 31, no. 5, pp. 1100–1109, Sep./Oct. 1995.

[19] Y. Hu, Z. Q. Zhu, and M. Odavic, "Comparison of two-individual current control and vector space decomposition control for dual three-phase PMSM," *IEEE Trans. Ind. Appl.*, vol. 53, no. 5, pp. 4483-4492, Sep./Oct. 2017.

[20] E. Levi, R. Bojoi, F. Profumo, H. A. Toliyat, and S. Williamson, "Multiphase induction motor drives - a technology status review," *IET Electr. Power Appl.*, vol. 1, no. 4, pp. 489-516, Jul. 2007.

[21] X. Zou, S. Huang, Z. Qin, X. Hu, and G. Kan, "A control method for permanent-magnet synchronous motor with unbalanced cable resistor," in *Proc. Int. Conf. Power Electron. Syst. Appl.*, 2015, pp. 1-3.

[22] S. D. Wilson, P. Stewart, and B. P. Taylor, "Methods of resistance estimation in permanent magnet synchronous motors for real-time thermal management," *IEEE Trans. Energy Convers.*, vol. 25, no. 3, pp. 698-707, Sep. 2010.

[23] B. Vaseghi, B. Nahid-Mobarakeh, N. Takorabet and F. Meibody-Tabar, "Experimentally validated dynamic fault model for PMSM with stator

winding inter-turn fault," *in Proc. IEEE Ind. Appl. Soc. Annu. Meeting*, 2008, pp. 1-5.

[24] R. Bojoi, F. Farina, M. Lazzari, F. Profumo, and A. Tenconi, "Analysis of the asymmetrical operation of dual three-phase induction machines," in *Proc. IEEE Int. Elect. Mach. Drives Conf.*, 2003, pp. 429-435.

[25] H. Ye, W. Song, Z. Ruan, and Y. Yan, "Current control methods for dual three-phase permanent magnet synchronous motors considering machine parameter asymmetry," in *Proc. Int. Conf. Elect. Mach. Syst.*, 2019, pp. 1-6.

[26] Y. Hu, Z. Q. Zhu, and M. Odavic, "Compensation of unbalanced impedance of asymmetric wind power PMSG compensated by external circuits in series," *CES Trans. Elect. Mach. Syst.*, vol. 1, no. 2, pp. 180-188, Jun. 2017.

[27] Y. Hu, Z. Q. Zhu, and M. Odavic, "Comparative study of current control methods of asymmetric PM synchronous machine," in *Proc. Int. Conf. Elect. Mach.*, 2016, pp. 982-988.

[28] A. H. Abosh and Z. Q. Zhu, "Current control of permanent magnet synchronous machine with asymmetric phases," in *Proc. IET Int. Conf. Power Electron., Mach. Drives,* 2014, pp. 1-6.

[29] P. Rioual, H. Pouliquen, and J. P. Louis, "Regulation of a PWM rectifier in the unbalanced network state using a generalized model," *IEEE Trans. Power Electron.*, vol. 11, no. 3, pp. 495-502, May 1996.

[30] J. Hu, and Y. He, "Modeling and control of grid-connected voltage-sourced converters under generalized unbalanced operation conditions," *IEEE Trans. Energy Convers.*, vol. 23, no. 3, pp. 903-913, Sep. 2008.

[31] Y. Zhao, and T. A. Lipo, "Modeling and control of a multi-phase induction machine with structural unbalance," *IEEE Trans. Energy Convers.*, vol. 11, no. 3, pp. 578-584, Sep. 1996.

[32] J. Hu, H. Nian, H. Xu, and Y. He, "Dynamic modeling and improved control of DFIG under distorted grid voltage conditions," *IEEE Trans. Energy Convers.*, vol. 26, no. 1, pp. 163–175, Mar. 2011.

[33] D. Ye, J. Li, R. Qu, H. Lu, and Y. Lu, "Finite set model predictive MTPA control with VSD method for asymmetric six-phase PMSM," in *Proc. IEEE Int. Elect. Mach. Drives Conf.*, 2017, pp. 1-7.

[34] J. Xu, M. Odavic, and Z. Zhu, "An advanced harmonic compensation strategy for dual three-phase permanent magnet synchronous machines considering different angle displacements," in *Proc. IEEE Energy Convers. Congr. Expo.*, 2019, pp. 1797-1803.

[35] A. H. Abosh, Z. Q. Zhu, and Y. Ren, "Reduction of torque and flux ripples in space vector modulation-based direct torque control of asymmetric permanent magnet synchronous machine," *IEEE Trans. Power Electron.*, vol. 32, no. 4, pp. 2976-2986, Apr. 2017.

[36] Y. Hu, Z. Q. Zhu, and M. Odavic, "Torque capability enhancement of dual three-phase PMSM drive with fifth and seventh current harmonics injection," *IEEE Trans. Ind. Appl.*, vol. 53, no. 5, pp. 4526–4535, Sep. 2017.

[37] V. Blasko, V. Kaura, and W. Niewiadomski, "Sampling of discontinuous voltage and current signals in electrical drives: A system approach," *IEEE Trans. Ind. Appl.*, vol. 34, no. 5, pp. 1123–1130, Sep./Oct. 1998.

[38] A. G.Yepes, F. D. Fernandez-Comesana, P. Malvar, J. Lopez, and J.Doval-Gandoy, "Torque ripple minimization in surface-mounted PM drives by means of PI + multi-resonant controller in synchronous reference frame," in *Proc. IEEE Annu. Conf. IEEE Ind. Electron. Soc.*, 2010, pp. 1017-1022.